

Isogeometric analysis based investigation on material filling of coin cavities

Cite as: AIP Advances 13, 035311 (2023); doi: 10.1063/5.0139826

Submitted: 23 December 2022 • Accepted: 13 February 2023 •

Published Online: 6 March 2023



View Online



Export Citation



CrossMark

Jing Li,¹ Tingyu Yan,² Qingyun Wang,² Jiangping Xu,^{2,a)} and Fei Wang^{3,b)}

AFFILIATIONS

¹School of Electronic Information and Electrical Engineering, Anyang Institute of Technology, Anyang City, Henan Province, China

²School of Mechanical Engineering, Jiangsu University, 301 Xuefu Road, Zhenjiang City, Jiangsu Province, China

³Shenyang Mint Company Limited, 138 Dadong Road, Dadong District, Shenyang City, Liaoning Province, China

^{a)}Author to whom correspondence should be addressed: jiangpingxu@ujs.edu.cn

^{b)}Electronic mail: symintwf@163.com

ABSTRACT

The coining technology produces a wide variety of commemorative coins with exquisite patterns. However, it often encounters defects such as insufficient filling, flash lines, light bands, and so on. Process engineers usually perform multiple tryouts to avoid the above-mentioned problems in actual production. This is not only time-consuming and laborious but also ineffective. The virtual tryout of the finite element method (FEM) could assist engineers to avoid the defects in the coining process with a great improvement in product quality. In order to exactly describe complex patterns of commemorative coins, a large number of elements are employed in the classical FEM. Even then, the three dimensional elements, which come in early contact with the reliefs of the punch/die, undergo large deformation and become distorted. Errors of contact judgment between the tools and the workpiece in the FEM occur during the simulation process. Taking into account the advantage of Non-Uniform Rational B-Spline (NURBS) basis functions when accurately describing complex boundaries or surfaces, isogeometric analysis (IGA) is developed for studying the material filling of coin cavities. Six numerical examples involving elastic and plastic analyses with/without contact issues are considered by the presented IGA frameworks and show good performance of the present method in simulating the cavity filling compared with ABAQUS. In addition, numerical findings also indicate that the proposed method exhibits excellent contact detection and strong anti-mesh distortion in large deformation of the coining process. These encouraging observations motivate us to explore the NURBS description of complicated reliefs of coins and the corresponding IGA framework for the coining process.

© 2023 Author(s). All article content, except where otherwise noted, is licensed under a Creative Commons Attribution (CC BY) license (<http://creativecommons.org/licenses/by/4.0/>). <https://doi.org/10.1063/5.0139826>

I. INTRODUCTION

Commemorative coins have been widely used in currency circulation and collection.^{1–3} However, formation defects such as insufficient filling, flash lines, and light bands are always encountered in the actual coining process.^{2,4,5} Generally, process engineers apply multiple real tryouts to alleviate the above-mentioned defects. However, this is not only time-consuming, laborious, and expensive but also lacks theoretical guidance. Virtual tryouts could be adopted to shorten the design period, reduce product cost, and improve product quality. At present, the most popular numerical method is the finite element method, but it is difficult to accurately describe the geometry of the contact surface between the die and the workpiece,

as shown in Fig. 1(a). As we know, in practical problems such as sheet metal forming, forging, ringing, and so on, the calculation of the normal vector at each node plays an important role in the contact algorithm. As shown in Fig. 1(a), the common node of two adjustment elements has two different normal vectors. This inevitably leads to a series of numerical difficulties or errors in contact analysis. The most common solution is to increase the number of elements to make the boundary smooth [see Fig. 1(b)]. However, this not only increases the computational cost but also does not fundamentally solve the problem. With the increasing complexity of patterns on the coin surface [see Fig. 1(c)], the requirements for calculation accuracy of modeling and numerical analysis are becoming higher. Traditional theories and methods have found it difficult to meet

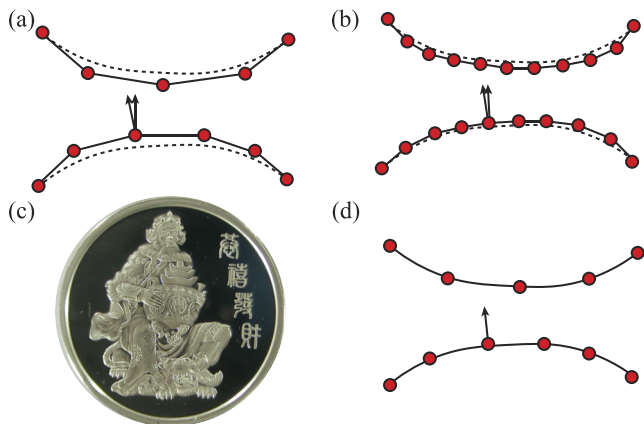


FIG. 1. Discretization of two curves by (a) coarse elements and (b) fine elements in the FEM. (c) Complex reliefs on the coin and (d) NURBS description of the two curves by using coarse knots in IGA. The calculation error of the normal vector vanishes by using IGA.

the requirements of designing complex-patterned coining parts. Therefore, seeking new theoretical and numerical methods for the coining process has an important practical engineering value of improving the product quality. In this study, the isogeometric analysis including the contact algorithm is adopted to analyze the performance of IGA in cavity filling between two objects. As shown in Fig. 1(d), the error of the normal vector is avoided in the framework of IGA.

In 2005, Hughes proposed isogeometric analysis to overcome the seamless integration of computer aided design (CAD) and computer aided engineering (CAE).⁶ In the concept of IGA, the description of the CAD model and interpolation in CAE adopt the same basis functions. Thus, modeling and simulation of engineering problems can be linked automatically. As an extension of the FEM, IGA takes NURBS basis functions as interpolation bases instead of Lagrange basis functions in the FEM. It naturally takes original the NURBS parametric surface patch as the element instead of the artificially divided element by other mesh generators. It should be mentioned that the control points of the NURBS parametric mesh are the carriers of physical variables and have the same function as nodes in the FEM. Due to the accuracy of the geometric description, IGA has been successfully applied to study plate and shell problems.^{7–9} Furthermore, because of any order partial derivative of the NURBS shape function, it fits for some problems with a higher-order partial derivative and partial differential equations, for example, fluid^{10–12} and fluid structure coupling problems, biomechanical systems,^{13–15} electromagnetism,^{16,17} and phase field.^{18,19} In addition, IGA applies the same basis functions to the process of modeling and analysis to realize the seamless integration of CAD/CAE, and it has been widely used in size optimization^{20,21} and shape optimization.^{22,23} Finally, it can preserve the geometric continuity and does not need meshing, so it is quite suitable for analyzing contact problems.^{24–29}

Contact analysis is still one of the difficult problems in computational mechanics, and it has always been the focus and hotspot of research.^{30–32} At present, the FEM is the traditional method for

coin simulation, but it still has the technical bottlenecks mentioned above. Scholars^{33–35} found that using IGA to study the contact problem would bring a lot of convenience. The most important one is that the FEM uses a non-smooth boundary to approach a smooth boundary, which leads to the non-smoothness of the contact boundary. In addition, there is only C^0 continuity between elements, so the normal vector is not unique [see Fig. 1(a)]. However, IGA retains the geometric continuity and the outer normal is unique [see Fig. 1(d)] so as to avoid the error of contact calculation. Therefore, the contact algorithm based on IGA has been greatly developed. Lu²⁵ established the basic framework of the 2D frictionless contact problem and deduced the segment-segment contact formula. De Lorenzis *et al.*^{26,27} explored the friction contact problem of large 2D and 3D deformation. Temizer²⁸ studied the frictionless contact problem of finite deformation and deduced the knot-segment formula. In the process of coining, materials are compressed to flow and fill numerous cavities of the punch and die and finally form the required shape of the coin, as demonstrated in Fig. 2. The workpiece is put on the lower die. The upper die (also called the punch) moves down with a velocity v controlled by a slider that connects with the press. The lower die is stationary. The interaction between the molds and the workpiece involves the complex contact nonlinear problem. In order to study the material filling of the cavities of dies, the contact method for rigid and deformable objects should be implemented. In this work, the IGA-based contact algorithm is presented to study the contact states of two objects, such as the punch and the workpiece, based on the NURBS advantage of exactly describing the geometries of the coins and tools. The characteristic of this paper is to make full use of the accuracy of IGA in multi-object contact judgment and its ability to resist mesh distortion. Through the research on the filling performance of IGA in the coining process, it will lay a theoretical foundation for the detailed study of IGA's work in the formation fields of the coinage industry in the future.

This paper is organized as follows: Sec. II describes the NURBS basis functions and numerical integration of IGA. In Sec. III, the elastic and elastic-plastic equilibrium equations of one object are derived, and the contact algorithm is embedded into the framework of IGA. Then, the equilibrium equations of two objects with the contact condition are established. In order to verify the performance of the IGA with/without the contact algorithm, six examples including elastic and elastic-plastic problems with one or two objects are studied in Sec. IV. Finally, we conclude with a summary in Sec. V.

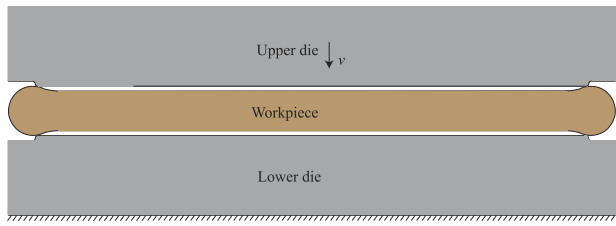


FIG. 2. Modeling of the coining process involving two typical tools, namely, the upper die and lower die.

II. BASIC FUNDAMENTAL OF ISOGEOMETRIC ANALYSIS

A. NURBS basis function

B-spline is convenient for geometrical modeling, but it cannot accurately describe some complex graphics, such as circles and ellipsoids. Usually, non-uniform rational B-spline is adopted in IGA as the basis function, which not only inherits the advantages of the B-spline basis but also overcomes its disadvantages.³⁶ Similar to the B-spline curve, for a given knot vector $\Xi = \{\xi_1, \xi_2, \dots, \xi_{n+p+1}\}$, the NURBS curve is defined as a linear combination of the NURBS basis functions,

$$C(\xi) = \sum_{i=1}^n R_{i,p}(\xi) P_i, \quad (1)$$

where $P = \{P_1, P_2, \dots, P_n\}$ is a vector of control points and $R_{i,p}(\xi)$ is the NURBS basis function, written as

$$R_{i,p}(\xi) = \frac{N_{i,p}(\xi) \omega_i}{\sum_{i=1}^n N_{i,p}(\xi) \omega_i}, \quad (2)$$

where $N_{i,p}(\xi)$ is i th B-spline basis function of order p and calculated by the Cox-de Boor recurrence formula³⁷ and ω_i is the i th weight factor. In the same way, the two given knot vectors $\Xi = \{\xi_1, \xi_2, \dots, \xi_{n+p+1}\}$ and $\Theta = \{\eta_1, \eta_2, \dots, \eta_{m+q+1}\}$, with $(m+1)$ ($n+1$) control points. Then the tensor-product NURBS surface is given by

$$S(\xi, \eta) = \sum_{i=1}^n \sum_{j=1}^m R_{i,j}(\xi, \eta) P_{ij}, \quad (3)$$

where P_{ij} is a net of control points and $R_{i,j}(\xi, \eta)$ is the bivariate basis function expressed as

$$R_{i,j}(\xi, \eta) = \frac{N_{i,p}(\xi) M_{j,q}(\eta) \omega_{ij}}{\sum_{i=1}^n \sum_{j=1}^m N_{i,p}(\xi) M_{j,q}(\eta) \omega_{ij}}, \quad (4)$$

where $M_{j,q}(\eta)$ is the B-spline basis function of order q and ω_{ij} is a net of weights.

Figure 3(a) shows an example of the NURBS surface with orders $p = q = 2$. The red points indicate the control points, and the dashed lines represent the control mesh. The two open knot vectors are $\Xi = \{0, 0, 0, 1/3, 2/3, 1, 1, 1\}$ and $\Theta = \{0, 0, 0, 1/3, 2/3, 1, 1, 1\}$. The multiplicities at both ends are $p + 1 = q + 1 = 3$. The knots divide the geometrical domain into 3×3 elements, as shown in **Fig. 3(b)**. The shape of the element is affected by the control points, knot vectors, and weight factors.

B. Numerical integration

Both the IGA and the classical FEM use the concept of isoparametric transformation for numerical integration.⁶ The difference is that the traditional FEM applies the Lagrange basis functions to approximate the problem domain while IGA accurately describes the geometric domain by using NURBS shape functions. From the three blue sub-domains in panels (a)–(c) of **Fig. 3**, it can be seen that there are three integral domains, namely, the physical domain Ω_e , parametric domain $\hat{\Omega}_e$, and parent domain $\bar{\Omega}_e$. The mapping relationships of the Gaussian integral in the elements among three spaces are given as

$$\int_{\Omega} f(x, y) d\Omega = \sum_{e=1}^{n_e} \int_{\Omega_e} f(x, y) d\Omega_e, \quad (5)$$

$$\begin{aligned} &= \sum_{e=1}^{n_e} \int_{\hat{\Omega}_e} f(x(\xi), y(\eta)) |\hat{J}| d\hat{\Omega}_e \\ &= \sum_{e=1}^{n_e} \int_{\bar{\Omega}_e} f(x(\bar{\xi}), y(\bar{\eta})) |\bar{J}| |\hat{J}| d\bar{\Omega}_e. \end{aligned} \quad (6)$$

As shown in **Fig. 3(a)**, the integral of $f(x, y)$ in the entire physical domain Ω is the sum of integrals over each element Ω_e . Then, it is mapped to the parameter domain $\hat{\Omega}_e$ through the first determinant of the mapping Jacobian $|\hat{J}|$,

$$|\hat{J}| = \frac{\partial x}{\partial \xi} \frac{\partial y}{\partial \eta} - \frac{\partial x}{\partial \eta} \frac{\partial y}{\partial \xi}. \quad (7)$$

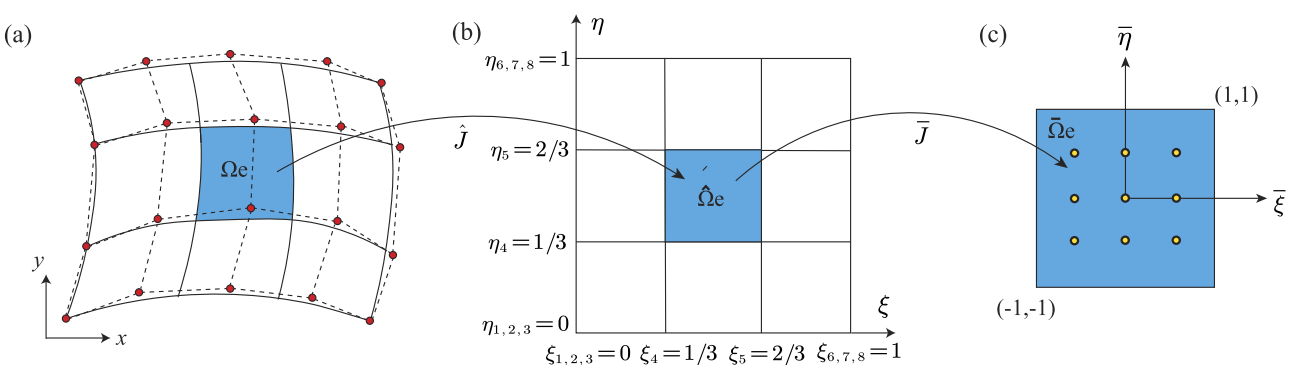


FIG. 3. Numerical integration in IGA. (a) The physical domain Ω_e contains both the physical mesh (solid lines) and the control polygon (dash lines). The red points represent the control points in IGA, which are similar to the nodes in the classical FEM that carry physical variables. (b) The parametric domain $\hat{\Omega}_e$ defines the elements. (c) The parent domain $\bar{\Omega}_e$ is a normalized element on which the Gauss quadrature is calculated. The yellow circles represent the Gauss points.

This can be calculated according to the coordinate mapping relation between the physical domain Ω_e and parametric domain $\hat{\Omega}_e$,

$$\begin{aligned} x &= \sum_{i=1}^n N_i(\xi) P_i, \\ y &= \sum_{j=1}^m N_j(\eta) P_j. \end{aligned} \quad (8)$$

The determinant of the second mapping Jacobian $|\tilde{J}|$ from the parametric domain $\hat{\Omega}_e$ to the parent domain $\bar{\Omega}_e$ is written as

$$|\tilde{J}| = 0.25(\xi_{i+1} - \xi_i)(\eta_{j+1} - \eta_j). \quad (9)$$

At the same time, the coordinate mapping between the parametric domain $\hat{\Omega}_e$ and the parent domain $\bar{\Omega}_e$ is

$$\begin{aligned} \xi &= 0.5[(\xi_{i+1} - \xi_i)\hat{\xi} + (\xi_{i+1} + \xi_i)], \\ \eta &= 0.5[(\eta_{j+1} - \eta_j)\hat{\eta} + (\eta_{j+1} + \eta_j)]. \end{aligned} \quad (10)$$

III. IGA-BASED NUMERICAL METHOD FOR MULTI-OBJECTS

The coining process involves large plastic deformation under the action of the upper die. In order to illustrate a clear procedure of application of IGA into the coining simulation, we address the theory equations obeying the elastic/plastic law for one and two objects without/with the contact algorithm.

A. Elastic problem of an object

The system potential energy for the elastic problem of one object³⁸ is simply defined as

$$\Pi = \Pi_e + \Pi_{ext} = \frac{1}{2} \int_{\Omega} \boldsymbol{\epsilon}^T \boldsymbol{\sigma} d\Omega - \int_{\Omega} \boldsymbol{\delta}^T \mathbf{b} d\Omega - \int_{\Gamma} \boldsymbol{\delta}^T \mathbf{t} d\Gamma, \quad (11)$$

where Π_e and Π_{ext} are the works carried out by the internal and external forces, respectively; \mathbf{b} is the body force; \mathbf{t} is the surface force; and $\boldsymbol{\epsilon}$, $\boldsymbol{\sigma}$, and $\boldsymbol{\delta}$ are the strain, stress, and displacement vectors of an arbitrary point in the problem domain, respectively. Substituting $\boldsymbol{\epsilon} = \mathbf{B}\mathbf{u}$, $\boldsymbol{\sigma} = \mathbf{D}\boldsymbol{\epsilon}$, and $\boldsymbol{\delta} = \mathbf{N}\mathbf{u}$ into Eq. (11) results in

$$\Pi = \frac{1}{2} \mathbf{u}^T \int_{\Omega} \mathbf{B}^T \mathbf{D} \mathbf{B} \mathbf{u} d\Omega - \mathbf{u}^T \int_{\Omega} \mathbf{N}^T \mathbf{b} d\Omega - \mathbf{u}^T \int_{\Gamma} \mathbf{N}^T \mathbf{t} d\Gamma, \quad (12)$$

where \mathbf{D} is the elastic matrix, \mathbf{B} is the strain gradient matrix, \mathbf{N} is the shape function, and \mathbf{u} is the displacement vector of the control point. According to the principle of minimum potential energy $\delta\Pi = 0$, the equilibrium equation can be written as

$$\mathbf{K}\mathbf{u} = \mathbf{F}, \quad (13)$$

where $\mathbf{K} = \int_{\Omega} \mathbf{B}^T \mathbf{D} \mathbf{B} d\Omega$ is the stiffness matrix and $\mathbf{F} = \int_{\Omega} \mathbf{N}^T \mathbf{b} d\Omega + \int_{\Gamma} \mathbf{N}^T \mathbf{t} d\Gamma$ is the nodal force vector.

B. Elastic-plastic problem of an object

1. Elastic-plastic equilibrium equation

The linear isotropic hardening law is adopted in this work and expressed as³⁹

$$\kappa(\tilde{\varepsilon}^P) = \sigma_0 + (1 - \beta)\tilde{H}\tilde{\varepsilon}^P, \quad \beta \in [0, 1], \quad (14)$$

where $\tilde{\varepsilon}^P$ is the equivalent plastic strain, σ_0 is the initial yield stress, \tilde{H} is a constant, and β is the Bauschinger factor for the isotropic hardening model. Given the yield stress, the classical von-Mises yield function⁴⁰ with flow rules can be expressed as

$$f(\eta, \tilde{\varepsilon}^P) = \|\eta\| - \sqrt{\frac{2}{3}}\kappa(\tilde{\varepsilon}^P), \quad (15)$$

where η is the shifted stress related to the hardening law. According to Eq. (15), if $f \leq 0$, the material becomes plastic.

Different from the elastic problem, the stress and strain are related to the loading history in the elastic-plastic problem.⁴¹⁻⁴³ Variables, such as stress, strain, and displacement, are expressed in the form of increments. Assuming a displacement increment $d\mathbf{u}$, the resulting strain increment $d\boldsymbol{\epsilon}$ decomposes into elastic and plastic strains,

$$d\boldsymbol{\epsilon} = d\boldsymbol{\epsilon}^e + d\boldsymbol{\epsilon}^p = \mathbf{D}^{-1} d\boldsymbol{\sigma} + d\lambda \frac{\partial f}{\partial \boldsymbol{\sigma}}, \quad (16)$$

where $d\boldsymbol{\epsilon}^e$ is the elastic strain matrix and $d\boldsymbol{\epsilon}^p$ is the plastic strain matrix. $d\lambda$ is called the plastic multiplier and equal to the increment in the effective plastic strain in the case of von Mises material. It can be determined by the consistency condition $f(\boldsymbol{\sigma} + d\boldsymbol{\sigma}, \lambda + d\lambda) = 0$ (see Ref. 44 for details). The stress increment $d\boldsymbol{\sigma}$ is obtained as

$$d\boldsymbol{\sigma} = \mathbf{D}_{ep} d\boldsymbol{\epsilon} = (\mathbf{D} - \mathbf{D}_p) d\boldsymbol{\epsilon}, \quad (17)$$

where \mathbf{D}_{ep} is the elastic-plastic matrix and \mathbf{D}_p is the plastic matrix.

Bringing Eqs. (16) and (17) into Eq. (11) and using the principle of minimum potential energy $\delta\Pi = 0$, the equilibrium equation for the elastic-plastic problem is written as

$$\mathbf{K}(\mathbf{u})\mathbf{u} = \mathbf{F}, \quad (18)$$

where the stiffness matrix is $\mathbf{K}(\mathbf{u}) = \int_{\Omega} \mathbf{B}^T \mathbf{D}_{ep} \mathbf{B} d\Omega$, which is a function of the displacement \mathbf{u} due to the history-related elastic-plastic matrix \mathbf{D}_{ep} .

2. Newton-Raphson iteration

The linear Eq. (13) can be solved without difficulty. In this work, the Newton-Raphson iterative method⁴⁵ is required to solve the nonlinear Eq. (18), which can be rewritten as

$$\mathbf{R}(\mathbf{u}) = \mathbf{K}(\mathbf{u})\mathbf{u} - \mathbf{F} = 0. \quad (19)$$

Using the first-order Taylor expanding formula, the solution increment is calculated by

$$\Delta\mathbf{u}^i = -\mathbf{R}^i(\mathbf{K}_T^i)^{-1} = (\mathbf{F} - \mathbf{K}(\mathbf{u}^i))(\mathbf{K}_T^i)^{-1}, \quad (20)$$

where \mathbf{R}^i is the residual force matrix and \mathbf{K}_T^i is the tangent stiffness matrix. i is the i th iteration number in the current load step. The force- and displacement-based termination criteria for iteration in the following numerical examples are expressed as

$$\text{conv} = \frac{\sum (R^i)^2}{1 + \sum (F^i)^2} \quad (21)$$

and

$$\text{conv} = \frac{\sum (\Delta u^i)^2}{1 + \sum (\Delta u^0)^2}, \quad (22)$$

respectively.

C. Elastic-plastic problem of two objects

In the process of coining, there are three rigid tools. One upper die is moving downward while the other two are stationary. For simplicity, the collar is neglected in this study. In order to describe the non-deformable property of the rigid tools, Young's modulus of the upper die (or the rigid objects of some cases in Sec. IV) is set to be 100 times of that of the deformable object.

1. Contact algorithm in ICA

The purpose of contact search⁴⁶ is to determine whether two parts are separated or in contact. As shown in Fig. 4(a), objects A and B are separated initially, whose configurations are Ω_0^A and Ω_0^B , respectively. Their boundaries are Γ_0^A and Γ_0^B , respectively. Then, they may come in contact with each other after some displacement Δ_A and Δ_B . Their new configurations are Ω_t^A and Ω_t^B and boundaries are Γ_t^A and Γ_t^B at time t , respectively. Herein, the segment-segment search algorithm is adopted for contact judgment due to the advantages of NURBS. The two contact boundaries are classified into master and slave segments. The master points are located on the master segment, and the slave points are located on the slave segment.^{47,48} The two in-contact segments of the two objects are defined as Γ_c^A and Γ_c^B , respectively.

Whether objects A and B come in contact with each other is judged mainly through two steps. The first step is to find the closest point on the master segment $\mathbf{C}(\xi)$ to the slave point \mathbf{x}^A . The problem can be described as shown in Fig. 4(b), where a slave point \mathbf{x}^A and a master segment $\mathbf{C}(\xi)$ are given. The closest point of \mathbf{x}^A is found, such as \mathbf{x}^{B1} , \mathbf{x}^{B2} , or \mathbf{x}^{B3} . According to the problem description, the candidate point should satisfy the following formula:

$$f(\xi) = (\mathbf{C}(\xi) - \mathbf{x}^A) \cdot \mathbf{t} = 0. \quad (23)$$

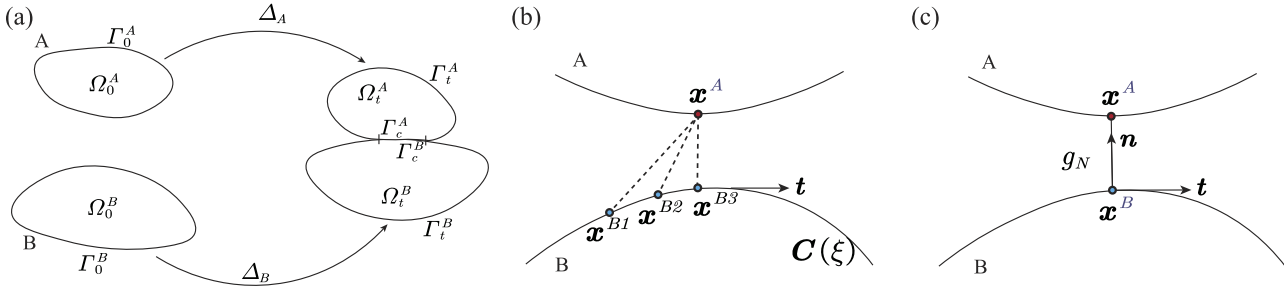


FIG. 4. (a) Contact configuration of two objects A and B. A is the contactor, and B is the target. Initially, they are at configurations Ω_0^A and Ω_0^B , respectively, far from each other. Their boundaries are Γ_0^A and Γ_0^B , respectively. Then, they may come in contact with each other after some displacement Δ_A and Δ_B . Their new configurations are Ω_t^A and Ω_t^B and boundaries are Γ_t^A and Γ_t^B at time t , respectively. The in-contact segments of the two objects are recorded as Γ_c^A and Γ_c^B , respectively. (b) The closest point is found on the master segment to \mathbf{x}^A . $\mathbf{C}(\xi)$ is the master segment parameterized in ξ . \mathbf{x}^{B1} , \mathbf{x}^{B2} , and \mathbf{x}^{B3} are the potential closest points of \mathbf{x}^A , and \mathbf{t} is the tangent. (c) The contact state is judged. \mathbf{x}^A is the real closest point of \mathbf{x}^A , and \mathbf{n} is the out normal.

Apparently from Fig. 4(b), it can be seen that the closest point of \mathbf{x}^A is \mathbf{x}^{B3} and the tangent vector at the nearest point is $\mathbf{t} = \mathbf{C}'(\xi) = d\mathbf{C}(\xi)/d\xi$. The Newton iteration method is usually used to solve Eq. (23) to find the nearest point, and the corresponding iterative equation is

$$H^k \Delta \xi^{k+1} = -[(\mathbf{C}(\xi) - \mathbf{x}^A) \cdot \mathbf{t}]^k. \quad (24)$$

Here, $H = \|\mathbf{C}'(\xi_i)\|^2 + \mathbf{C}''(\xi_i) \cdot (\mathbf{C}(\xi_i) - \mathbf{x}^A)$ is the Hessian matrix, and the second derivative of $\mathbf{C}(\xi)$ is $\mathbf{C}''(\xi) = d^2\mathbf{C}(\xi)/d\xi^2$. The corresponding increment is given as

$$\Delta \xi = -\frac{(\mathbf{C}(\xi) - \mathbf{x}^A) \cdot \mathbf{C}'(\xi)}{\mathbf{C}'(\xi) \cdot \mathbf{C}'(\xi) + (\mathbf{C}(\xi) - \mathbf{x}^A) \cdot \mathbf{C}''(\xi)}. \quad (25)$$

The second step is to judge the contact state of the two objects. As illustrated in Fig. 4(c), the closest point of \mathbf{x}^A is \mathbf{x}^B whose outward normal is \mathbf{n} . We define a gap function between two points \mathbf{x}^A and \mathbf{x}^B as

$$g_N = (\mathbf{x}^A - \mathbf{x}^B) \cdot \mathbf{n} = \begin{cases} > 0, & \text{separation,} \\ \leq 0, & \text{contact.} \end{cases} \quad (26)$$

According to Eq. (26), if $g_N \leq 0$, the two segments contact; otherwise, they separate.

2. Equilibrium equation with the contact algorithm

According to the literature,²⁵ we adopt the penalty formulation for frictionless contact analysis, and the whole potential energy of the system for contact analysis is expressed as

$$\Pi = \Pi_e + \Pi_{ext} + \Pi_c, \quad (27)$$

where the contact potential energy is defined as

$$\Pi_c = \frac{1}{2} \int_{\Gamma_c} p g_N d\Gamma_c, \quad (28)$$

where p is the Lagrangian multiplier and \mathbf{g}_N is the gap function and can be calculated using Eq. (26). This paper adopts penalty regulation that replaces the multiplier with a penalty factor,

$$\Pi_c = \frac{1}{2} \int_{\Gamma_c} \varepsilon \langle -\mathbf{g}_N \rangle^2 d\Gamma_c. \quad (29)$$

Here, $\langle \cdot \rangle$ is the Macaulay bracket and only counts the contact part into the integral. The variation form of Π_c is

$$\delta\Pi_c = \int_{\Gamma_c} \varepsilon \mathbf{g}_N \delta \mathbf{g}_N d\Gamma_c. \quad (30)$$

Furthermore,

$$\delta\Pi_c = \int_{\Gamma_c} \varepsilon (\mathbf{x}^A - \mathbf{x}^B) \cdot (\delta \mathbf{x}^A - \delta \mathbf{x}^B) d\Gamma_c. \quad (31)$$

According to the definition of NURBS Eq. (1), the two points \mathbf{x}^A and \mathbf{x}^B can be expressed as

$$\mathbf{x}^A = \sum_{i=1}^{n_p^A} N_i^A(\xi) P_i^A, \quad \mathbf{x}^B = \sum_{j=1}^{n_p^B} N_j^B(\eta) P_j^B, \quad (32)$$

where n_p^A and n_p^B are the number of control points on the contact boundaries Γ_c^A and Γ_c^B , respectively.

Combining Eqs. (1), (2), (26), (29), and (32) and applying the principle of minimum potential energy $\delta\Pi = 0$, the final equilibrium equation is given as

$$\begin{aligned} \mathbf{K}\mathbf{u} = [\mathbf{K}_g + \mathbf{K}_c]\mathbf{u} &= \begin{bmatrix} \mathbf{K}_1 + \boldsymbol{\alpha}_{11} & \boldsymbol{\alpha}_{12} \\ \boldsymbol{\alpha}_{21} & \mathbf{K}_2 + \boldsymbol{\alpha}_{22} \end{bmatrix} \begin{bmatrix} \mathbf{u}_1 \\ \mathbf{u}_2 \end{bmatrix} \\ &= \begin{bmatrix} \mathbf{F}_1 \\ \mathbf{F}_2 \end{bmatrix} = \mathbf{F}, \end{aligned} \quad (33)$$

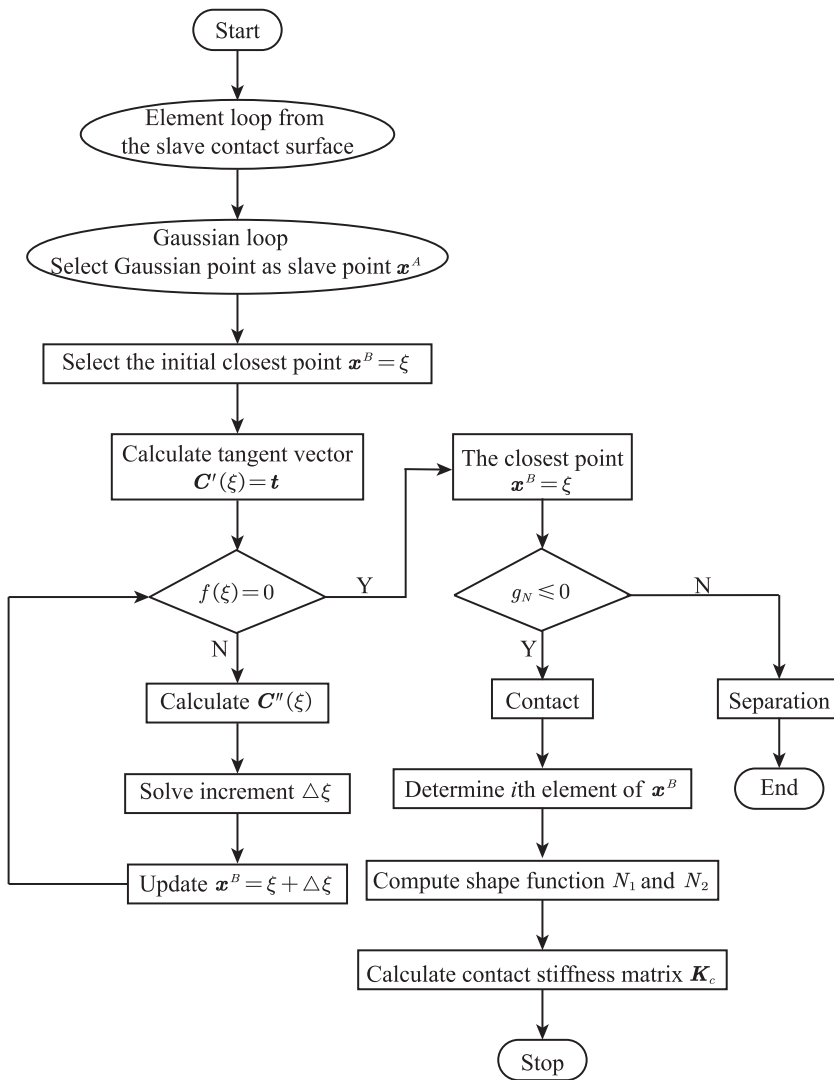


FIG. 5. Process of contact search and judgment in IGA.

where the geometric stiffness matrix \mathbf{K}_g can be obtained by Eq. (13) or Eq. (18) and the contact stiffness matrix \mathbf{K}_c can be obtained by taking the second derivative of contact potential energy Π_c to the displacement \mathbf{u} . The specific calculation formula is given as

$$\mathbf{K}_c = \frac{\partial^2 \Pi_c}{\partial \mathbf{u}^2} = \begin{bmatrix} \alpha_{11} & \alpha_{12} \\ \alpha_{21} & \alpha_{22} \end{bmatrix} = \begin{bmatrix} \varepsilon \int N_1^T N_1 d\Gamma_c^1 & -\varepsilon \int N_1^T N_2 d\Gamma_c^1 \\ -\varepsilon \int N_2^T N_1 d\Gamma_c^1 & \varepsilon \int N_2^T N_2 d\Gamma_c^1 \end{bmatrix}. \quad (34)$$

It is worth noting that although the penalty function method has many advantages, the penalty factor ε is artificially selected, and its value directly affects the calculation accuracy of the contact stiffness matrix \mathbf{K}_c . Theoretically, the larger the value of ε , the smaller the allowable penetration of the contact surface, and the higher the calculation accuracy of \mathbf{K}_c . However, when ε is too large, there will be some disadvantages, such as difficult convergence or large fluctuation of \mathbf{K}_c . The procedure of contact search and judgment is given in Fig. 5.

IV. NUMERICAL RESULTS

In this section, six examples, including the elastic and elastic-plastic problems of one and two objects, are analyzed. The first two examples are used to test the calculation efficiency and accuracy of elastic and elastic-plastic IGA. Then, the wheel-plate example is used for verifying the contact algorithm of IGA in this work. Considering the various kinds of patterns on the surfaces of the punch and die, three different geometries of the punch are adopted, and one real coin workpiece is used. In order to verify the superiority of IGA, the results of IGA obtained by MATLAB codes are compared with those of the FEM got from ABAQUS. The reference results for comparison purpose are obtained either from the theoretical formula or ABAQUS where more elements are implemented. Note that the relative errors calculated in the following examples are given as $|c - c_r|/c_r \times 100\%$, where c is the value of the physical variable obtained from the FEM or IGA and c_r is the reference value from the FEM with very rich elements. Due to different solvers such as MATLAB-based IGA and ABAQUS, especially because the solving method in ABAQUS is optimized, the computational efficiency is not compared directly. However, the

freedom of the final solving system is adopted for efficiency comparison. The units of length and stress in all examples are mm and MPa, respectively, for both FEM and IGA.

A. Elastic plate with a hole

In order to verify the calculation accuracy of IGA, the problem of the infinite plate with a central hole, known as stress concentration,⁴⁹ is selected. Considering the symmetry of the problem structure, only a quarter of the geometry is modeled, as shown in Fig. 6. The dimension of the length $l = 20$ and the radius of the circular hole $r = 1$ are shown in panel (a). The material is low-carbon steel. Its Young's modulus and Poisson's ratio are $E = 200 \times 10^3$ and $\nu = 0.25$, respectively. The origin of the coordinate system is set at the center of the hole. The right and bottom edges are constrained in x and y directions, respectively. The left edge is subjected to a uniform load $q_c = 30$, as illustrated in panel (b). The original FEM model is discretized into $n_{ele} = 2 \times 1$ in ABAQUS [see panel (a)], and the same discretization scheme is also used in IGA [see panel (b)]. In the case of IGA, as illustrated in Figs. 6(b), 2×1 elements and 12 control points are plotted. The knot vectors are $\Xi = \{0 \ 0 \ 0 \ 1 \ 2 \ 2 \ 2\}/2$ and $\Theta = \{0 \ 0 \ 0 \ 1 \ 1 \ 1\}$, and the orders of the basis functions are $p = 2$ and $q = 2$. For a better comparison of IGA and the FEM, different meshing schemes with more elements are applied. Then, their results are compared with the theoretical solution. Assuming an infinite length l , the exact stress $\sigma_{xx}|_{x=0}$ at the right edge is expressed as

$$\sigma_{xx}|_{x=0} = \frac{q_c}{2} \left(2 + \frac{r^2}{R^2} + 3 \frac{r^4}{R^4} \right), |y| \geq r, \quad (35)$$

where R is the distance from a point at the edge to the center of the circle.

The panels in the first and second rows of Fig. 7 plot the x -displacement u_x and x -stress σ_{xx} , respectively. The results in the first and second columns are obtained from the FEM with the element number $n_{ele} = 540$ and IGA with elements $n_{ele} = 512$, respectively. As can be seen from panels (a) and (b), the magnitude of the displacement tends to increase linearly from right to left, and the maximum values in both cases are -2.80×10^{-3} . We also notice that the maximum stresses in both cases appear at point $x = 0$ and $y = r$. According to Eq. (35), the theoretical solution of stress at point $(0, r)$ is $\sigma_{xx}|_{(x=0,y=r)} = q_c (2 + r^2/r^2 + 3r^4/r^4)/2 = 3q_c = 90$.

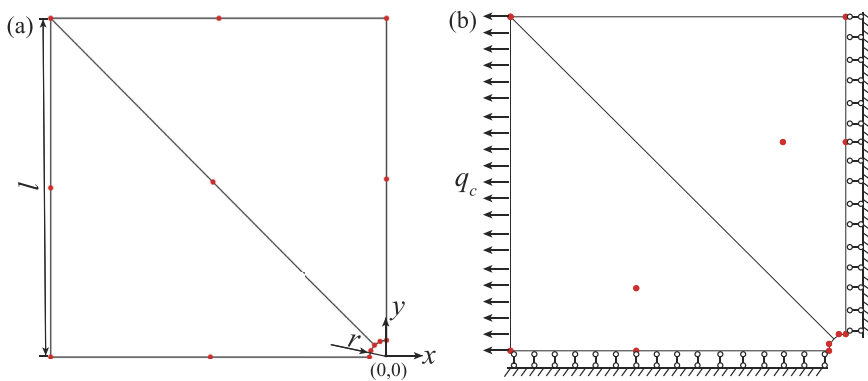


FIG. 6. Geometry and meshes of the elastic plate with a hole. (a) Meshes with 2×1 elements in the FEM, where the red points are nodes. The length of the square plate is l , and the radius of the hole is r . (b) Boundary conditions and meshes with 2×1 elements in the IGA case. The red points are control points. The dimensions are $l = 20$ and $r = 1$. The right and bottom edges are constrained in x and y directions, respectively. The left edge is subjected to a uniform load $q_c = 30$.

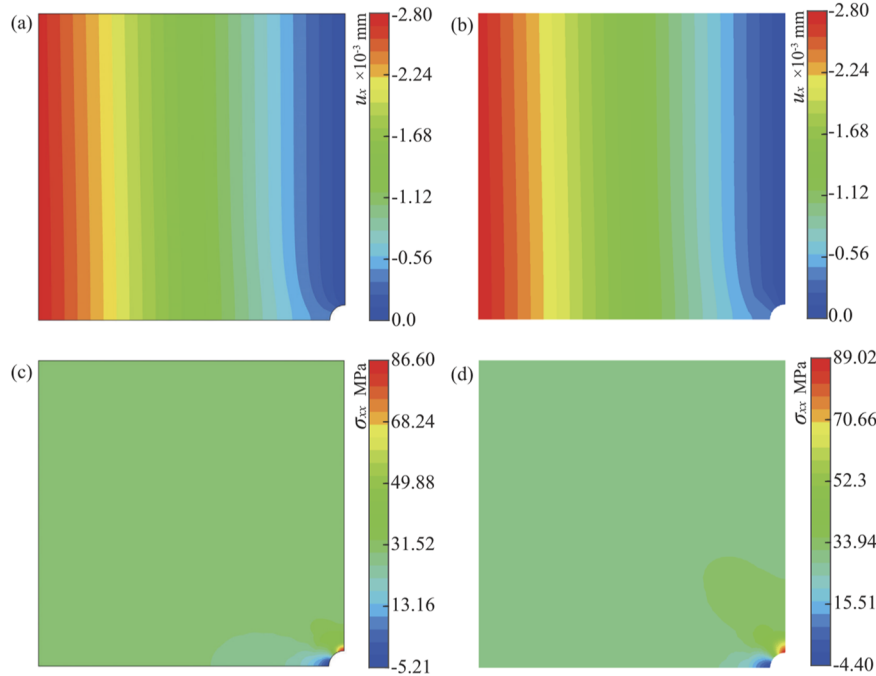


FIG. 7. Overlay plots of x -displacement u_x of (a) the FEM with $n_{ele} = 540$ and (b) IGA with $n_{ele} = 512$. Stress σ_{xx} of (c) the FEM with $n_{ele} = 540$ and (d) IGA with $n_{ele} = 512$. n_{ele} is the number of elements.

Both the FEM and IGA produce similar outputs close to the exact solution.

In order to get further quantitative comparisons of the FEM and IGA in this case, five different meshing schemes are conducted. The number of elements and nodes in each mesh for the FEM and IGA is listed in Table I. As can be seen from the table, the relative errors of both cases decrease as element numbers increase. Moreover, the error of IGA with 512 elements is just 1.09%, which is much smaller than the 3.78% of the FEM with 540 elements. We also notice that in this meshing scheme, the number of IGA is $n_{conpts} = 612$, which is almost twice less than that in the FEM with nodal number $n_{nodes} = 1717$. In some sense, we can conclude that the computational efficiency of IGA is better than that of the FEM (in this work, we do not compare the efficiency of the two methods in detail due to implementing different solvers). In addition, $\sigma_{xx}|_{(x=0,y=r)}$ of IGA converges to the theoretical solution faster than the FEM, as shown in Fig. 8.

TABLE I. Stress $\sigma_{xx}|_{(x=0,y=r)}$ comparison between the FEM and IGA under different element numbers.

FEM				IGA			
n_{ele}	n_{nodes}	σ_{xx}	err (%)	n_{ele}	n_{conpts}	σ_{xx}	err (%)
2	13	39.55	56.06	2	12	45.13	49.86
8	37	46.72	48.09	8	24	62.26	30.82
32	121	66.11	26.54	32	60	68.74	23.62
112	381	68.74	23.62	128	180	79.06	12.16
540	1717	86.60	3.78	512	612	89.02	1.09

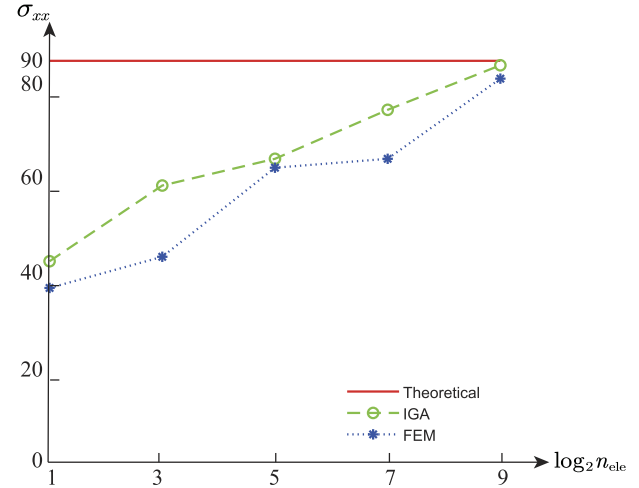


FIG. 8. Stress $\sigma_{xx}|_{(x=0,y=r)}$ curves over the element number between the FEM and IGA. The red solid line represents the theoretical solution while the green dash and blue dotted lines are results from IGA and the FEM, respectively. The x-axis represents the number of elements n_{ele} , and the y-axis represents stress $\sigma_{xx}|_{(x=0,y=r)}$.

B. Elastic-plastic bolt connection

Bolts are commonly used in mechanical engineering, and proper pre-tightening force can improve the reliability and service life of bolt connections.^{50–52} In this example, elastic-plastic IGA is programmed to analyze the stress distribution under a certain pre-tightening force. The geometry and modeling of the bolt are

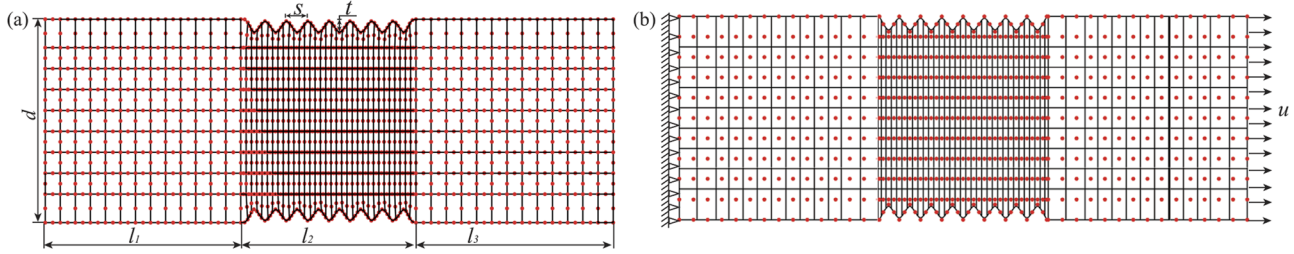


FIG. 9. Geometry and meshes of the bolt. (a) Dimensions and meshes with 59×9 elements in the FEM. The dimensions are $l_1 = l_3 = 10$, $l_2 = 8$, $d = 10$, $s = 1.05$, and $t = 0.562$. (b) Boundary conditions and meshes with 59×9 elements in IGA. The left edge is clamped, and the right edge is subjected to a horizontal displacement $u = 1.66 \times 10^{-2}$. The middle point of the left edge is set as the origin of the coordinate system.

illustrated in Fig. 9. The geometric dimensions are set as follows: smooth screw length $l_1 = l_3 = 10$, screw thread length $l_2 = 8$, major diameter $d = 10$, thread groove width $s = 1.05$, and thread height $t = 0.562$, as illustrated in panel (a). The middle point of the left edge is set as the origin of the coordinate system. The material is steel No. 45, whose Young's modulus $E = 210 \times 10^3$, Poisson's ratio $\nu = 0.31$, initial yield stress $\sigma_0 = 300$, and Bauschinger factor $\beta = 0$. The plastic modulus takes a value of $H = E/1000$. The force-based termination criterion for the Newton–Raphson iteration is chosen [see Eq. (21)]. The left end is clamped, and the right end is subjected to a horizontal displacement $u = 1.66 \times 10^{-2}$, as described in Fig. 9(b). A computational mesh composed of 531 elements is both used in the FEM [panel (a)] and IGA [panel (b)].

As illustrated in Fig. 9(b), the model is discretized by 59×9 quadratic elements with 693 control points. The knot vectors are

$\Xi = \{0\ 0\ 0.5\ 2\ 3\ 4\ 5\ 6\ 7\ 8\ 9\ 10\ 11\ 12.5\ 13\ 13\ 14\ 15\ 16\ 17\ 18\ 19\ 20\ 21\ 22\ 23\ 24\ 25\ 26\ 27\ 28\ 29\ 30\ 31\ 32\ 33\ 34\ 35\ 36\ 37\ 38\ 39\ 40\ 41\ 42\ 43\ 44\ 45\ 46\ 46.5\ 48\ 49\ 50\ 51\ 52\ 53\ 54\ 55\ 56\ 57\ 58.5\ 59\ 59\ 59\}/59$ and $\Theta = \{0\ 0\ 1\ 2\ 3\ 4\ 5\ 6\ 7\ 8\ 9\ 9\ 9\}/9$, respectively. Meanwhile, the FEM also adopts 59×9 quadratic elements with 1730 nodes [see Fig. 9(a)]. It is worth noting that when the number of elements is the same, the number of nodes in ABAQUS is almost three times the number of control points in IGA. This results from the important advantage of IGA that the NURBS basis function is C^1 continuous across the element boundary while the Lagrange basis function is C^0 continuous even when quadratic elements are used in the FEM.⁴⁰ For comparison purposes, the bolt is also meshed with $100 \times (59 \times 9)$ elements in ABAQUS for getting reference results.

From the results in panels (a)–(c) of Fig. 10, we notice that their maximum displacement are the same as the prescribed

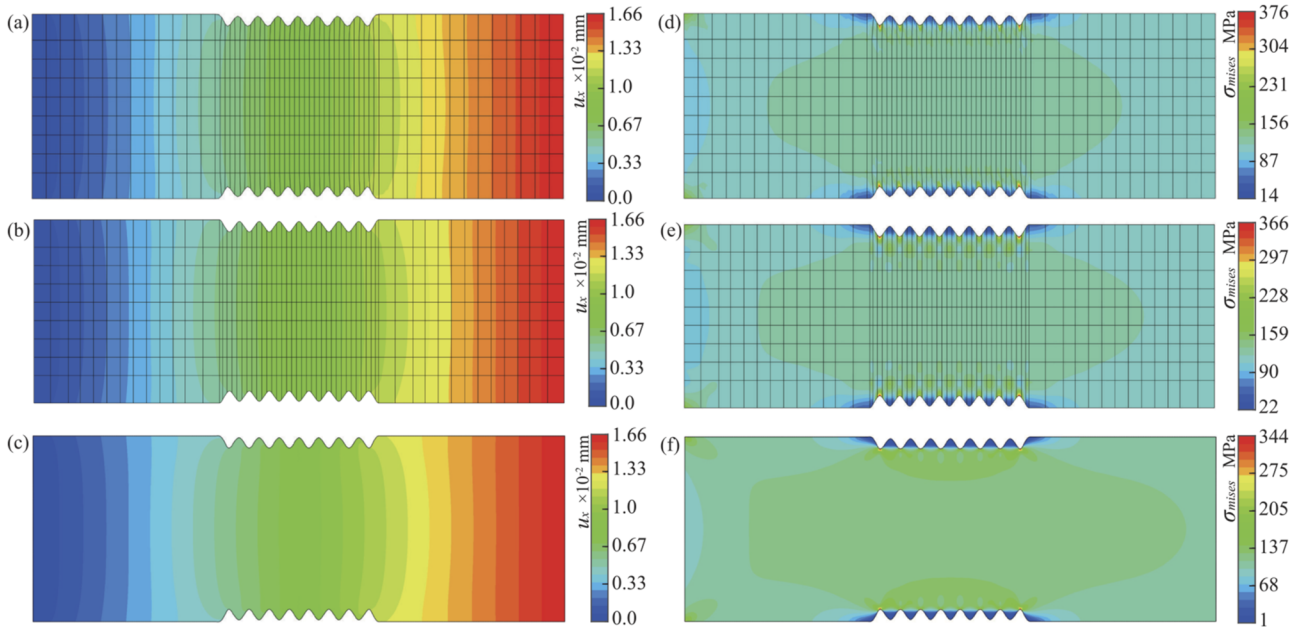


FIG. 10. Overlay plots of x-displacement u_x of (a) the FEM and (b) IGA with $n_{ele} = 59 \times 9$ elements and (c) the FEM with $n_{ele} = 100 \times (59 \times 9)$ elements; von-Mises stress σ_{mises} of (d) the FEM and (e) IGA with $n_{ele} = 59 \times 9$ elements and (f) the FEM with $n_{ele} = 100 \times (59 \times 9)$ elements. The meshes in the third row are hidden for a better view.

displacement 1.66×10^{-2} at the right edge and the distribution trend in all cases almost linearly increases from left to right. Comparing the stress plots in panels (d), (e), and (f), we find that the plot in panel (e) is very closer to the reference plot in panel (f). In addition, the maximum stress takes place at the bottom of the groove, whose x - and y -coordinates are $x = l_1 + l_2 - s/2$ and $y = \pm(d/2 - t)$, respectively. The value in the case of the FEM is 376, resulting in a relative error of 9%. In addition, it is 366 in IGA, leading to an error of only 6%. Due to the geometric property of the bolt, stress concentrations occur at the thread transition and root, while the stress at the top of the thread is obviously small. It means that when the bolt is subjected to lateral force, the thread transition and root will yield first and enter the stage of plastic deformation before other regions. Similarly, these two regions are also the structures that mainly bear force and cause failure first. With the help of IGA, a few elements required can obtain reasonable output for engineers to observe the relationship of stress distribution and pre-tightening force.

C. Wheel-plate elastic contact

This example is different from the two examples mentioned above where only one object is involved. In this and the following examples, we will study the local coining of two objects step by step with IGA in which contact judgment is embedded. In this test, an elastic contact problem is studied first. As shown in Fig. 11, a wheel-plate contact simulation is carried out. The object mentioned below is a deformable workpiece of a square plate, and the top object is a rigid punch represented by a wheel. The dimensions [in panel (a)] of the plate are length $l = 6$ and height $h = 2$, and those of the punch are inner radius $R = 3$ and thickness $T = 1$. In addition, the initial distance between the two objects is $h_0 = 0.01$. The material of workpiece is aluminum, whose Young's modulus is $E = 70 \times 10^3$ and Poisson's ratio is $\nu = 0.33$. The bottom edge of the workpiece is clamped, and the top punch is subjected to a vertical displacement $u = -0.5$ [see panel (b)]. The penalty factor is chosen as $\varepsilon = 1 \times 10^9$. As plotted in Fig. 11, the workpiece is discretized with a computational mesh composed of 10×4 elements

in both cases of the FEM and IGA. The other meshing scheme with $30 \times (10 \times 4)$ elements for the workpiece is used for getting reference results. The punch is represented by 3×3 elements in the case of IGA and shows the exact geometry of the wheel. The punch is considered as a discrete rigid tool in ABAQUS. Thus, more elements are needed to maintain geometric continuity and smoothness, as shown in panel (a).

As illustrated in Fig. 11(b), the workpiece is meshed with 10×4 quadratic elements with 72 control points in IGA. The knot vectors are $\Xi_w = \{0\ 0\ 0\ 0.75\ 1.5\ 2.65\ 3.8\ 5\ 6.2\ 7.35\ 8.5\ 9.25\ 10\ 10\ 10\}/10$ and $\Theta_w = \{0\ 0\ 0\ 1\ 2\ 3\ 4\ 4\ 4\}/4$, respectively. The punch is discretized into 3×3 quadratic elements with 25 control points, and the corresponding knot vectors are $\Xi_p = \Theta_p = \{0\ 0\ 0\ 1\ 2\ 3\ 3\ 3\}/3$.

In this and the following contact examples, the distributions of displacement and stress in the punch are not plotted in the cases of the FEM since the punch is rigid and has no deformation. However, they are illustrated in the case of IGA because the punch is considered as a deformable body with the Young's modulus 100 times of that of the workpiece. As illustrated in Figs. 12(a)–12(c), we can see that the displacement contour and places of maximum value in IGA agree very well with the reference solutions. A similar conclusion of stress results can be drawn from panels (d)–(f). Taking the maximum stresses 2.11×10^4 in panel (f) as a reference and 1.90×10^4 in panel (d) and 1.96×10^4 in panel (e) for comparison, the IGA obtains a relative error of 7%, which is less than that of the FEM, approximately 10%. The above-mentioned observations show better performance of IGA than the FEM with the same element number. Panels (g)–(i) are used to test the performance of the contact algorithm based on IGA. Even though the FEM uses more elements to describe the punch than IGA, the contact surfaces in panel (g) still show visible penetration while there is no visible penetration in panels (h) and (i), particularly in the red dashed boxes.

In Sec. III C 2, we briefly introduce the influence of the penalty factor ε on the contact stiffness matrix K_c . Herein, we will observe the effect of ε on the maximum von-Mises stress σ_{mises} . As shown in Fig. 13, small ε leads to extremely small contact force. Thus, the object does not undergo deformation, and σ_{mises} is very small.

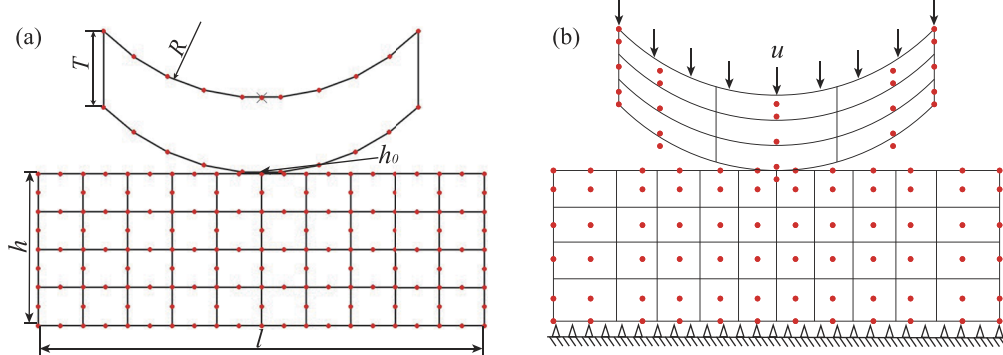


FIG. 11. Geometry and meshes of the wheel-plate contact problem. (a) Dimensions and meshes with 10×4 elements for the workpiece in the FEM. The length and height of the workpiece are $l = 6$ and $h = 2$, respectively. The dimensions of the punch are $R = 3$ and $T = 1$. The distance between the punch and workpiece is initially set to $h_0 = 0.01$. (b) Boundary conditions and meshes with 10×4 for the workpiece and 3×3 elements for the wheel in IGA. The bottom end of the workpiece is clamped, and the wheel is subjected to a vertical displacement $u = -0.5$.

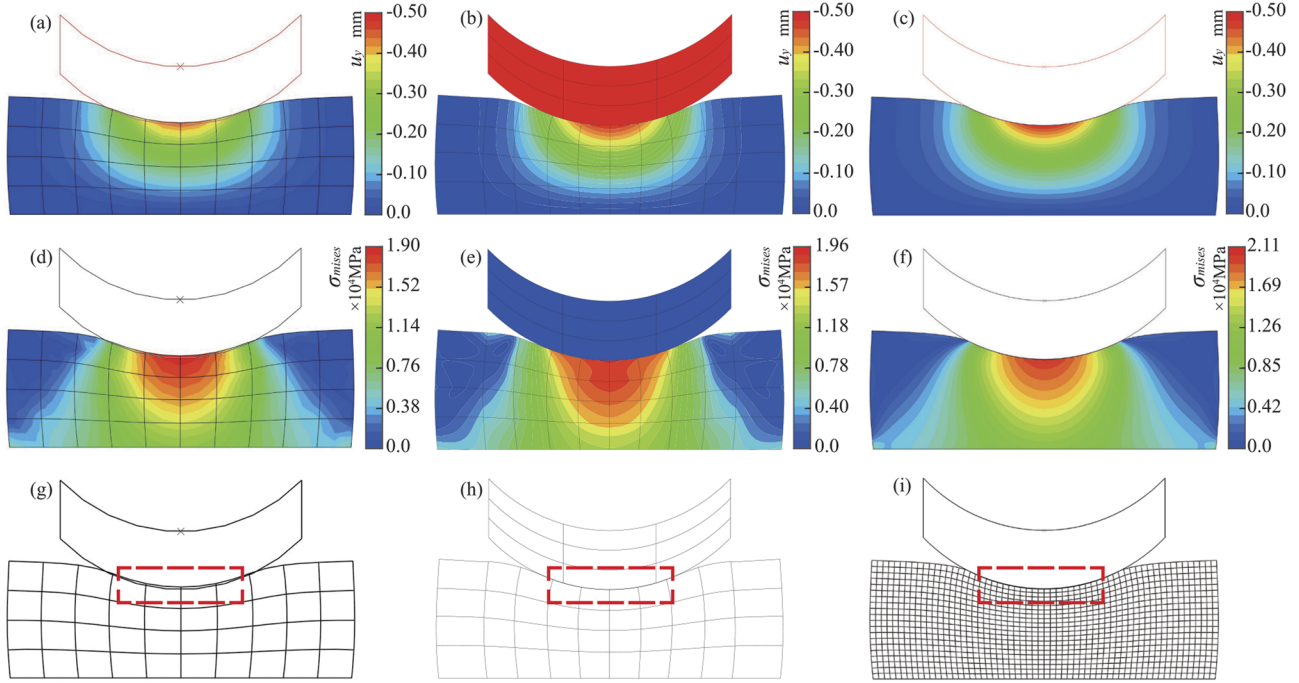


FIG. 12. Overlay plots of y -displacement u_y of (a) the FEM and (b) IGA with $n_{ele} = 10 \times 4$ and (c) the FEM with $n_{ele} = 30 \times (10 \times 4)$. von-Mises stress σ_{mises} of (d) the FEM and (e) IGA with $n_{ele} = 10 \times 4$ and (f) the FEM with $n_{ele} = 30 \times (10 \times 4)$. Deformed meshes of (g) the FEM and (h) IGA $n_{ele} = 10 \times 4$ and (i) the FEM with $n_{ele} = 30 \times (10 \times 4)$ elements. The distributions of displacement and stress in the punch are not plotted in cases of the FEM since the punch is rigid and has no deformation while they are illustrated in the case of IGA because the punch is considered a deformable body with the Young's modulus 100 times of that of the workpiece.

As ε increases, a higher calculation accuracy of the contact force is achieved. Thus, more accurate stresses are obtained. Of course, too large ε does not significantly improve the calculation accuracy and unfortunately leads to instability of contact judgment. In this case, $\varepsilon = 1 \times 10^9$ is enough to get satisfied results.

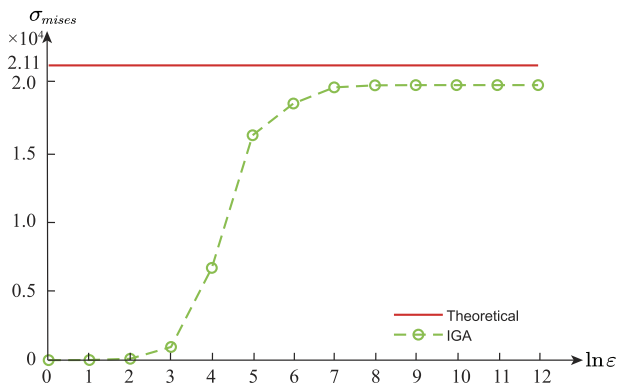


FIG. 13. Influence of the penalty factor ε on maximum von-Mises stress σ_{mises} in IGA. The red solid line represents the reference solution in the FEM with $n_{ele} = 30 \times (10 \times 4)$ elements, and the green dashed line indicates the IGA results. The x- and y-axes represent the values of the penalty factor ε and the maximum von-Mises stresses σ_{mises} , respectively.

D. Wave-plate elastic-plastic contact

This example is used to analyze the filling of materials in the elastic-plastic problem. As shown in Fig. 14, a punch whose bottom has two small waves compresses a regular plate. The dimensions of the model are length $l = 10$ and height $h = 5$ for the workpiece and length $L = 9$, height $H = 3$, wave width $S = 5$, and wave depth $T = 0.625$ for the punch, and the minimum distance between them is $h_0 = 0.05$, as shown in panel (a). The material of the workpiece is Au, whose Young's modulus $E = 79 \times 10^3$, Poisson's ratio $\nu = 0.4$, initial yield stress $\sigma_0 = 88$, plastic modulus $H = E/100$, and Bauschinger factor $\beta = 0$. The bottom end of the workpiece is clamped, and the top end of the punch is subjected to a vertical displacement $u = -1$, as shown in panel (b). The penalty factor takes a value of $\varepsilon = E \times 10^5$, and the displacement-based termination criterion is chosen [see Eq. (22)]. Discrete rigidness is employed to construct the punch, and the workpiece is discretized into 12×12 elements with 481 nodes in ABAQUS [see panel (a)]. As presented in panel (b), 6×6 and 12×12 elements for the punch and workpiece, respectively, are employed in IGA. The punch mesh has 64 control points. The orders of basis are $p_p = q_p = 2$. The knot vectors are $\Xi_p = \Theta_p = \{0 \ 0 \ 0 \ 1 \ 2 \ 3 \ 3 \ 3\}/3$. The workpiece mesh has 196 control points. The orders of the basis functions are $p_w = q_w = 2$. The knot vectors are $\Xi_w = \Theta_w = \{0 \ 0 \ 0 \ 1 \ 2 \ 3 \ 4 \ 5 \ 6 \ 7 \ 8 \ 9 \ 10 \ 11 \ 12 \ 12 \ 12\}/12$.

There are two wave peaks of the workpiece that are always in contact with the punch during the whole compression process. Thus, the displacements in these two regions are larger than

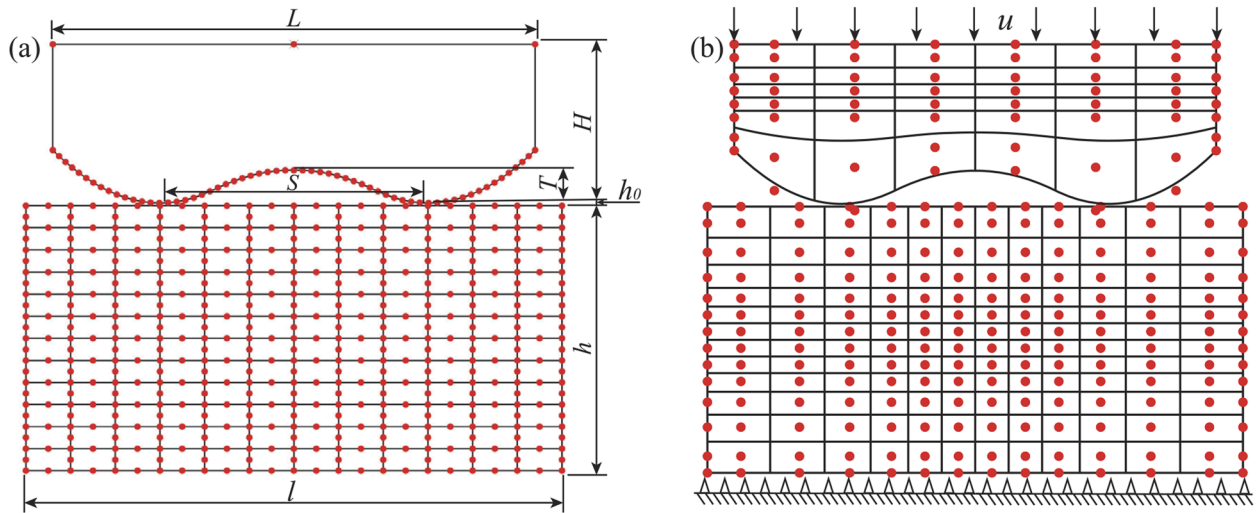


FIG. 14. Geometry and meshes of the wave-plate contact problem. (a) Dimensions and meshes with 12×12 elements for the workpiece in the FEM. The dimensions are $l = 10$ and $h = 5$ for the workpiece and $L = 9$, $H = 3$, $S = 5$, and $T = 0.625$ for the punch, and the minimum distance between the two objects is $h_0 = 0.05$. (b) Boundary conditions and meshes with 12×12 for the workpiece and 6×6 elements for the punch in IGA. The bottom end of the workpiece is clamped, and the top end of the punch is subjected to a vertical displacement $u = -1$.

others, as shown in panels (a)–(c) of Fig. 15. For comparison purpose, a fine mesh of 65×65 elements for the workpiece is implemented in the FEM, as shown in panel (c). We can see that the results from IGA are very close to the reference while the FEM with 12×12 elements produces a coarse output. In order to get a better view of the contact states and material filling, deformed meshes in the three cases are plotted in panels (d)–(f). The penetration

and incomplete material filling are obviously observed in the case of the FEM with 12×12 elements in panel (d) while no obvious defects are found in the case of IGA with the same element number and the FEM with 65×65 elements [see panels (e) and (f)]. Due to the robust contact algorithm in IGA, the materials are closely in contact with the punch boundary and fill the cavity of the tool very well.

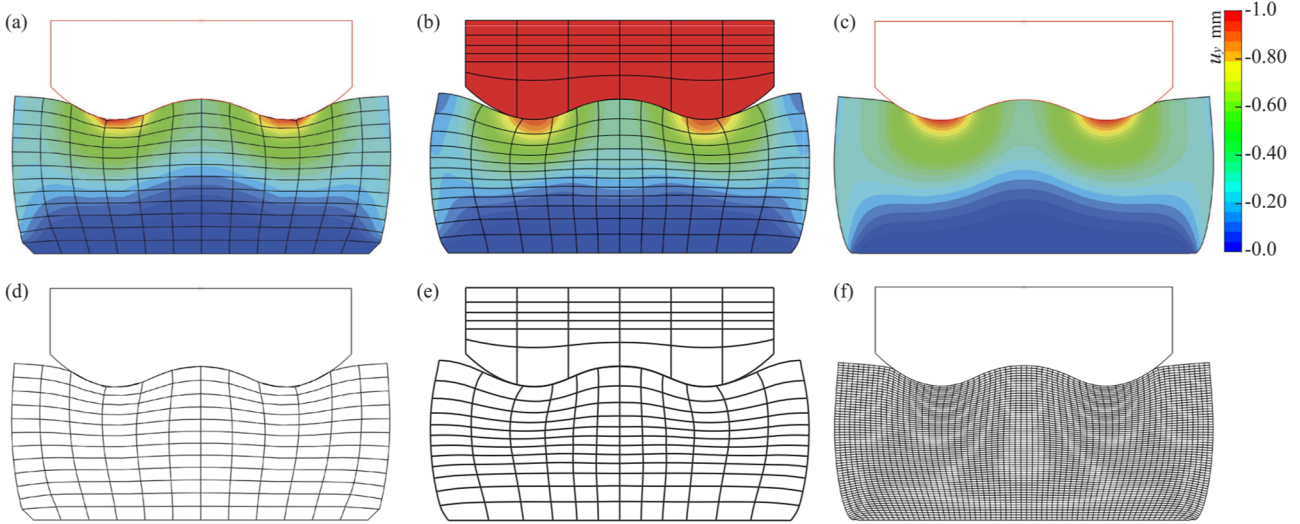


FIG. 15. Overlay plots of y -displacement u_y of (a) the FEM and (b) IGA with $n_{ele} = 12 \times 12$ and (c) the FEM with $n_{ele} = 30 \times (12 \times 12)$. Deformed meshes of (d) the FEM and (e) IGA with $n_{ele} = 12 \times 12$ and (f) the FEM with $n_{ele} = 30 \times (12 \times 12)$.

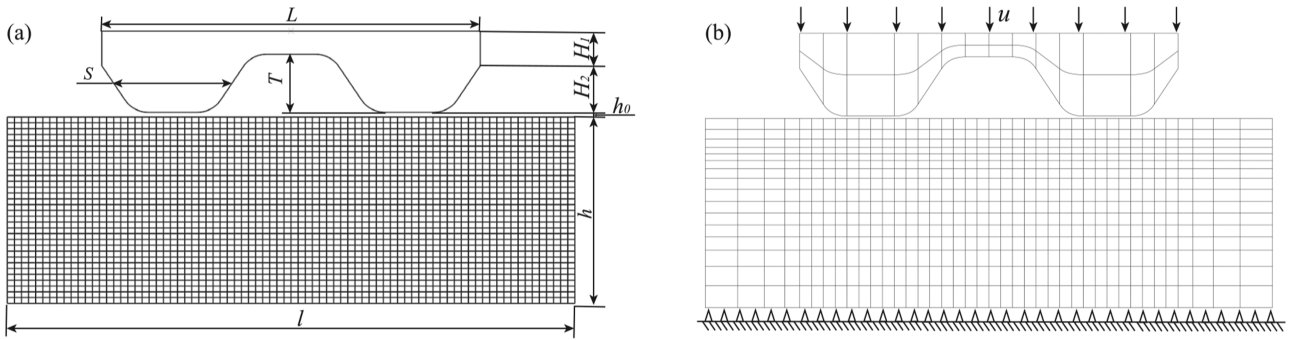


FIG. 16. Geometry and meshes of the channel-plate problem. (a) Dimensions and meshes with 80×32 elements for the workpiece in the FEM. The dimensions are length $l = 24$ and height $h = 8$ for the workpiece and length $L = 16$, heights $H_1 = 1.5$ and $H_2 = 2$, channel width $S = 5$, and depth $T = 2.5$ for the punch; the minimum distance between the two bodies is $h_0 = 0.1$. (b) Boundary conditions and meshes with 40×16 for the workpiece and 14×2 elements for the punch in IGA. The bottom end of the workpiece is clamped, and the top end of the punch is subjected to a vertical displacement $u = -3$. Nodes in panel (a) and control points in panel (b) are hidden for a better view.

E. Channel-plate elastic-plastic contact

Compared with the previous example, we mainly increase the wave depth of the punch to check the cavity filling of the materials. Considering that partial surfaces of the coin are flat, the wave peaks are replaced with flat regions, as shown in Fig. 16. These kinds of structures are usually designed to test the filling functions in the micro-coining process.^{53,54} The geometric dimensions are length $l = 24$ and height $h = 8$ for the workpiece and length $L = 16$, heights $H_1 = 1.5$ and $H_2 = 2$, channel width $S = 5$, and depth $T = 2.5$ for the punch. The minimum distance between the two objects is $h_0 = 0.1$, as shown in panel (a) of Fig. 16. The material of the workpiece is Ag, whose Young's modulus $E = 82 \times 10^3$, Poisson's ratio $\nu = 0.38$, initial yield stress $\sigma_0 = 50$, plastic modulus $H = E/100$, and Bauschinger factor $\beta = 0$. The bottom end of the workpiece is clamped, and the top end of the punch is subjected to a vertical displacement $u = -3$, as illustrated in panel (b). The penalty factor is set to $\epsilon = E \times 10^5$, and the displacement-based termination criterion is adopted [see Eq. (22)]. The punch and workpiece are meshed with 28 and 640 elements in IGA, respectively. Considering the better performance of IGA than FEM in the above-mentioned examples, finer mesh for the plate in the FEM is adopted in this example [see panel (a)].

Nodes in Fig. 16(a) and control points in Fig. 16(b) are hidden for a better view. In IGA, the workpiece is meshed with 40×16 elements and 756 control points. The orders of the basis functions are $p_w = q_w = 2$, and the knot vectors are $\Xi_w = \{0\ 0\ 0\ 1\ 2\ 3\ 4\ 5\ 6\ 7\ 8\ 9\ 10\ 11\ 12\ 13\ 14\ 15\ 16\ 17\ 18\ 19\ 20\ 21\ 22\ 23\ 24\ 25\ 26\ 27\ 28\ 29\ 30\ 31\ 32\ 33\ 34\ 35\ 36\ 37\ 38\ 39\ 40\ 40\ 40\}/40$ and $\Theta_w = \{0\ 0\ 0\ 1\ 2\ 3\ 4\ 5\ 6\ 7\ 8\ 9\ 10\ 11\ 12\ 13\ 14\ 15\ 16\ 16\}/16$, respectively. The punch is discretized by 14×2 elements and 84 control points. The order of the basis functions is $p_p = 2$ and $q_p = 1$, and the knot vectors are $\Xi_p = \{0\ 0\ 0\ 1\ 1\ 2\ 2\ 3\ 3\ 4\ 4\ 5\ 5\ 6\ 6\ 7\ 8\ 8\ 9\ 9\ 10\ 10\ 11\ 11\ 12\ 12\ 13\ 13\ 14\ 14\ 14\}/14$ and $\Theta_p = \{0\ 0\ 1\ 2\ 2\}/2$, respectively. In ABAQUS, the workpiece has 2560 quadratic elements and 7905 nodes.

As demonstrated in Fig. 17, even the number of elements in the FEM is four times that of IGA, and we can still see penetration in the FEM [see the penetration in the zoomed region of panel (a)]. However, there is no penetration in the same zoomed region in the case of IGA. In addition, several elements undergo distortion in the case of the FEM because of the large deformation in this example. However, the distortion meshes are not found in the case of IGA. These two advantages of robust contact judgment and immunity of distortion make IGA have further potential application in coining simulation.

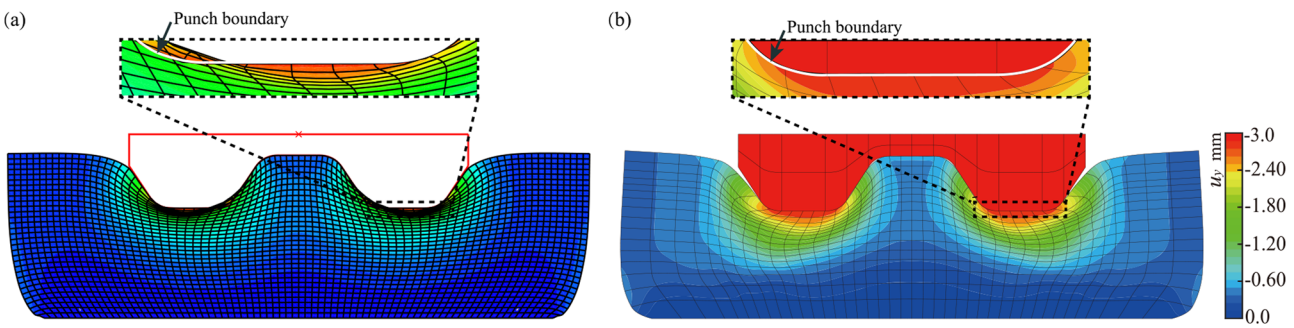


FIG. 17. Overlay plots of y -displacement u_y and deformed meshes of (a) the FEM with $n_{ele} = 40 \times 16 \times 4$ and (b) IGA with $n_{ele} = 40 \times 16$.

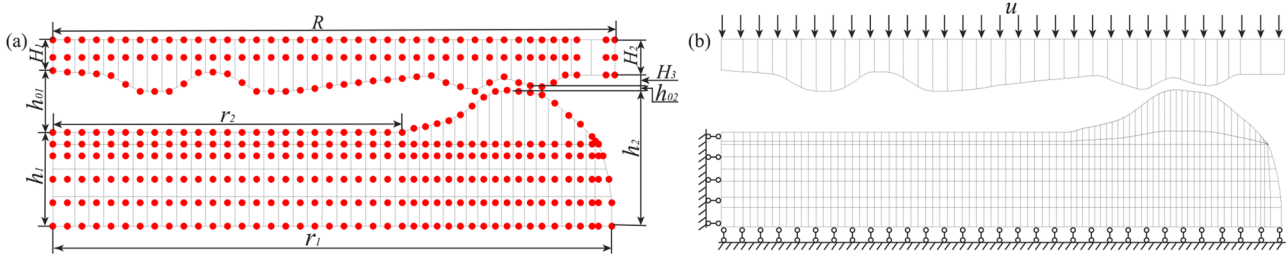


FIG. 18. Geometry and meshes in IGA. (a) Dimensions and simplified meshes with 41×4 and 38×1 elements. The dimensions include $r_1 = 9.6$, $r_2 = 6$, $h_1 = 1.6$, and $h_2 = 2.32$ for the workpiece and $R = 9.65$, $H_1 = 0.525$, $H_2 = 0.6$, and $H_3 = 0.19$ for the punch. The maximum and minimum distances between them are $h_{01} = 1.055$ and $h_{02} = 0.07$, respectively. (b) Boundary conditions and h -refinement meshes with 82×8 quadratic elements for the workpiece and 38×1 elements for the punch. The left and bottom ends of the workpiece are constrained in x and y directions, respectively, and the top end of the punch is subjected to a vertical displacement $u = -1.1$. Control points in panel (b) are hidden for a better view.

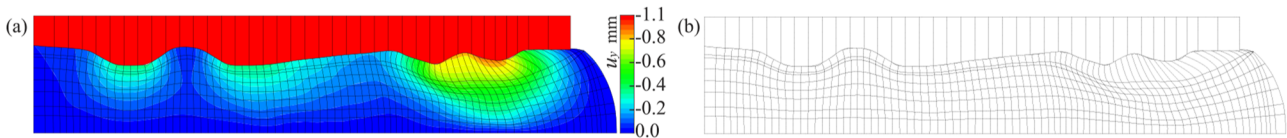


FIG. 19. Overlay plots of (a) y -displacement u_y and (b) deformed meshes in IGA with $n_{ele} = 82 \times 8$.

F. Coining simulation with real geometry of a coin workpiece

In this example, a real coin workpiece is adopted to explore the performance of IGA in simulating the coining process. As demonstrated in Fig. 18(a), only a quarter of the cross section of the coin is used due to the symmetric property. The related dimensions are radii $r_1 = 9.6$ and $r_2 = 6$ and heights $h_1 = 1.6$ and $h_2 = 2.32$ for the workpiece and radius $R = 9.65$ and heights $H_1 = 0.525$, $H_2 = 0.6$, and $H_3 = 0.19$ for the punch. The maximum and minimum distances between the two objects are $h_{01} = 1.055$ and $h_{02} = 0.07$, respectively. The material of the workpiece is Ag, whose Young's modulus is $E = 82 \times 10^3$, Poisson's ratio is $\nu = 0.38$, initial yield stress is $\sigma_0 = 50$, plastic modulus is $H = E/100$, and Bauschinger factor is $\beta = 0$. The left and bottom ends of the workpiece are constrained in x and y directions, respectively, and the top end of the punch is subjected to a vertical displacement $u = -1.1$, as described in panel (b). The penalty factor is set to $\epsilon = 10^5 \times E$, and the displacement-based termination criterion is used [see Eq. (22)]. As shown in panel (a), the workpiece initially adopts 164 quadratic uniform elements whose knot vectors are $\Xi_w = \{0\ 0\ 0\ 1\ 2\ 3\ 4\ 5\ 6\ 7\ 8\ 9\ 10\ 11\ 12\ 13\ 14\ 15\ 16\ 17\ 18\ 19\ 20\ 21\ 22\ 23\ 24\ 25\ 26\ 27\ 28\ 29\ 30\ 31\ 32\ 33\ 34\ 35\ 36\ 37\ 38\ 39\ 40\ 41\ 41\ 41\}/41$ and $\Theta_w = \{0\ 0\ 0\ 0.5\ 2\ 3.9\ 4\ 4\ 4\}/4$, respectively. Then, the workpiece is refined into 656 elements. The punch has 38×1 elements and 120 control points with a basis order of 2. The corresponding knot vectors are $\Xi_p = \{0\ 0\ 0\ 1\ 2\ 3\ 4\ 5\ 6\ 7\ 8\ 9\ 10\ 11\ 12\ 13\ 14\ 15\ 16\ 17\ 18\ 19\ 20\ 21\ 22\ 23\ 24\ 25\ 26\ 27\ 28\ 29\ 30\ 31\ 32\ 33\ 34\ 35\ 36\ 37\ 38\ 38\ 38\}/38$ and $\Theta_p = \{0\ 0\ 0\ 1\ 1\ 1\}$, respectively.

When observing the pair of contact boundaries of the punch and the workpiece, it can be seen that materials in the right convex region of the coin experience large deformation because they come in contact with the punch boundary earlier than others do [see Fig. 19(a)]. As plotted in Fig. 19(a), parts of the

materials are compressed to form the cavities of the coin, and some are extruded backward to form bulges. By checking the deformed meshes in panel (b), we notice that meshes in these deformed regions exhibit good anti-distortion ability. In addition, the boundary elements that come in contact with the punch show no obvious penetration.

V. CONCLUSION

Numerical methods can predict the deficiency of insufficient filling in practical coin products so as to optimize the coining process. However, the FEM uses Lagrange elements to describe the complex boundaries of the tools and the workpiece. These lead to inaccuracy of the contact algorithm and mesh-distortion that both result in bad performance of the FEM. Of course, mesh adaptive technology and refined meshes might solve the problems, but computation efforts are increased, and extra algorithms are required. Considering the advantages of NURBS basis functions in accurately describing the complex boundaries/surfaces and potential seamless integration of CAD/CAE, isogeometric analysis embedding the contact algorithm is proposed to study the material filling in the coining process. Several important conclusions have been drawn, as shown below:

- Better performance. Using the same element number, IGA produces smaller relative errors than the FEM (see examples in Secs. IV A–IV C). In addition, the degree of freedom of the final equations in IGA is much less than that in the FEM with the same number of elements (sometimes twice less, see example in Sec. IV D).
- Robust contact judgment. No obvious penetration is observed in elastic-plastic problems in the case of IGA, as demonstrated in examples of Secs. IV C–IV F.

- Strong anti-distortion. IGA possesses anti-mesh-distortion ability, as illustrated in examples of Secs. IV E and IV F. We notice that the meshes are distorted severely in the case of the FEM while no distortion is found in IGA.

Although IGA shows good capability of simulating the coining process and much work has been done at present, there is still critical research to be carried out, for example, introducing a collar into the framework of IGA and extending it to real 3D coining. Furthermore, the NURBS description of real coins, punches, dies, and collars is still a challenge due to the extremely complicated patterns.

ACKNOWLEDGMENTS

This work was supported by the Senior Talent Foundation of Jiangsu University (Grant No. 19JDG022) and the fund from Shenyang Mint Cooperative Limited (Grant No. 20220056).

AUTHOR DECLARATIONS

Conflict of Interest

The authors have no conflicts to disclose.

Author Contributions

Jing Li: Conceptualization (lead); Formal analysis (equal); Writing – original draft (equal); Writing – review & editing (equal). **Tingyu Yan:** Data curation (equal); Formal analysis (equal); Methodology (equal); Validation (equal); Visualization (equal); Writing – original draft (equal). **Qingyun Wang:** Data curation (equal); Validation (equal); Visualization (equal). **Jiangping Xu:** Conceptualization (equal); Formal analysis (equal); Funding acquisition (equal); Methodology (equal); Supervision (equal); Writing – review & editing (equal). **Fei Wang:** Methodology (equal); Validation (equal); Visualization (equal); Writing – review & editing (equal).

DATA AVAILABILITY

The data that support the findings of this study are available from the corresponding author upon reasonable request.

REFERENCES

- ¹J. Xu, Y. Liu, S. Li, and S. Wu, “Fast analysis system for embossing process simulation of commemorative coin–coinform,” *Comput. Model Eng. Sci.* **38**, 201–215 (2008).
- ²J. Xu, K. A. Khan, and T. El Sayed, “A novel method to alleviate flash-line defects in coining process,” *Precis. Eng.* **37**, 389–398 (2013).
- ³Q. Li, W. Zhong, Y. Liu, M. Zhang, and Z. Zhang, “Application of strain gradient plasticity in coining simulations of commemorative coins,” *Int. J. Mech. Sci.* **133**, 65–72 (2017).
- ⁴J. Xu, X. Chen, W. Zhong, F. Wang, and X. Zhang, “An improved material point method for coining simulation,” *Int. J. Mech. Sci.* **196**, 106258 (2021).
- ⁵Y. Peng, J. Xu, and Y. Wang, “Predictions of stress distribution and material flow in coining process for bi-material commemorative coin,” *Mater. Res. Express* **9**, 066505 (2022).
- ⁶T. J. R. Hughes, J. A. Cottrell, and Y. Bazilevs, “Isogeometric analysis: CAD, finite elements, NURBS, exact geometry and mesh refinement,” *Comput. Methods Appl. Mech. Eng.* **194**, 4135–4195 (2005).
- ⁷J. Kiendl, K.-U. Bletzinger, J. Linhard, and R. Wüchner, “Isogeometric shell analysis with Kirchhoff-Love elements,” *Comput. Methods Appl. Mech. Eng.* **198**, 3902–3914 (2009).
- ⁸J. Kiendl, Y. Bazilevs, M.-C. Hsu, R. Wüchner, and K.-U. Bletzinger, “The bending strip method for isogeometric analysis of Kirchhoff-Love shell structures comprised of multiple patches,” *Comput. Methods Appl. Mech. Eng.* **199**, 2403–2416 (2010).
- ⁹D. J. Benson, Y. Bazilevs, M.-C. Hsu, and T. J. R. Hughes, “A large deformation, rotation-free, isogeometric shell,” *Comput. Methods Appl. Mech. Eng.* **200**, 1367–1378 (2011).
- ¹⁰Y. Bazilevs, V. M. Calo, Y. Zhang, and T. J. R. Hughes, “Isogeometric fluid-structure interaction analysis with applications to arterial blood flow,” *Comput. Mech.* **38**, 310–322 (2006).
- ¹¹Y. Zhang, Y. Bazilevs, S. Goswami, C. L. Bajaj, and T. J. R. Hughes, “Patient-specific vascular NURBS modeling for isogeometric analysis of blood flow,” *Comput. Methods Appl. Mech. Eng.* **196**, 2943–2959 (2007).
- ¹²I. Akkerman, Y. Bazilevs, C. E. Kees, and M. W. Farthing, “Isogeometric analysis of free-surface flow,” *J. Comput. Phys.* **230**, 4137–4152 (2011).
- ¹³Y. Bazilevs, V. M. Calo, T. J. R. Hughes, and Y. Zhang, “Isogeometric fluid-structure interaction: Theory, algorithms, and computations,” *Comput. Mech.* **43**, 3–37 (2008).
- ¹⁴G. Xu, B. Mourrain, R. Duvigneau, and A. Galligo, “A new error assessment method in isogeometric analysis of 2D heat conduction problems,” *Adv. Sci. Lett.* **10**, 508–512 (2012).
- ¹⁵J. Xu, G. Vilanova, and H. Gomez, “Full-scale, three-dimensional simulation of early-stage tumor growth: The onset of malignancy,” *Comput. Methods Appl. Mech. Eng.* **314**, 126–146 (2017).
- ¹⁶A. Buffa, G. Sangalli, and R. Vázquez, “Isogeometric analysis in electromagnetics: B-splines approximation,” *Comput. Methods Appl. Mech. Eng.* **199**, 1143–1152 (2010).
- ¹⁷R. Vázquez and A. Buffa, “Isogeometric analysis for electromagnetic problems,” *IEEE Trans. Magn.* **46**, 3305–3308 (2010).
- ¹⁸H. Gómez, V. M. Calo, Y. Bazilevs, and T. J. R. Hughes, “Isogeometric analysis of the Cahn–Hilliard phase-field model,” *Comput. Methods Appl. Mech. Eng.* **197**, 4333–4352 (2008).
- ¹⁹L. Chen, B. Li, and R. de Borst, “Adaptive isogeometric analysis for phase-field modeling of anisotropic brittle fracture,” *Int. J. Numer. Methods Eng.* **121**, 4630–4648 (2020).
- ²⁰P. Phung-Van, C. H. Thai, M. Abdel-Wahab, and H. Nguyen-Xuan, “Optimal design of FG sandwich nanoplates using size-dependent isogeometric analysis,” *Mech. Mater.* **142**, 103277 (2020).
- ²¹H. Liu, D. Yang, X. Wang, Y. Wang, C. Liu, and Z.-P. Wang, “Smooth size design for the natural frequencies of curved Timoshenko beams using isogeometric analysis,” *Struct. Multidiscip. Optim.* **59**, 1143–1162 (2019).
- ²²N. D. Manh, A. Evgrafov, A. R. Gersborg, and J. Gravesen, “Isogeometric shape optimization of vibrating membranes,” *Comput. Methods Appl. Mech. Eng.* **200**, 1343–1353 (2011).
- ²³W. A. Wall, M. A. Frenzel, and C. Cyron, “Isogeometric structural shape optimization,” *Comput. Methods Appl. Mech. Eng.* **197**, 2976–2988 (2008).
- ²⁴K. A. Fischer and P. Wriggers, “Frictionless 2D contact formulations for finite deformations based on the mortar method,” *Comput. Mech.* **36**, 226–244 (2005).
- ²⁵J. Lu, “Isogeometric contact analysis: Geometric basis and formulation for frictionless contact,” *Comput. Methods Appl. Mech. Eng.* **200**, 726–741 (2011).
- ²⁶L. De Lorenzis, İ. Temizer, P. Wriggers, and G. Zavarise, “A large deformation frictional contact formulation using NURBS-based isogeometric analysis,” *Int. J. Numer. Methods Eng.* **87**, 1278–1300 (2011).
- ²⁷L. De Lorenzis, P. Wriggers, and G. Zavarise, “A mortar formulation for 3D large deformation contact using NURBS-based isogeometric analysis and the augmented Lagrangian method,” *Comput. Mech.* **49**, 1–20 (2012).
- ²⁸İ. Temizer, P. Wriggers, and T. J. R. Hughes, “Contact treatment in isogeometric analysis with NURBS,” *Comput. Methods Appl. Mech. Eng.* **200**, 1100–1112 (2011).

- ²⁹I. Temizer, P. Wriggers, and T. J. R. Hughes, “Three-dimensional mortar-based frictional contact treatment in isogeometric analysis with nurbs,” *Comput. Methods Appl. Mech. Eng.* **209–212**, 115–128 (2012).
- ³⁰M. Barboteu, K. Bartosz, and P. Kalita, “A dynamic viscoelastic contact problem with normal compliance, finite penetration and nonmonotone slip rate dependent friction,” *Nonlinear Anal.: Real World Appl.* **22**, 452–472 (2015).
- ³¹A. P. S. Selvadurai and A. Katrebi, “An adhesive contact problem for an incompressible non-homogeneous elastic halfspace,” *Acta Mech.* **226**, 249–265 (2015).
- ³²V. L. Popov and M. Heß, *Method of Dimensionality Reduction in Contact Mechanics and Friction* (Springer, 2015).
- ³³M. Stadler, G. A. Holzapfel, and J. Korelc, “Cn continuous modelling of smooth contact surfaces using NURBS and application to 2D problems,” *Int. J. Numer. Methods Eng.* **57**, 2177–2203 (2003).
- ³⁴J.-Y. Kim and S.-K. Youn, “Isogeometric contact analysis using mortar method,” *Int. J. Numer. Methods Eng.* **89**, 1559–1581 (2012).
- ³⁵R. Dimitri, L. De Lorenzis, M. A. Scott, P. Wriggers, R. L. Taylor, and G. Zavarise, “Isogeometric large deformation frictionless contact using T-splines,” *Comput. Methods Appl. Mech. Eng.* **269**, 394–414 (2014).
- ³⁶V. P. Nguyen, C. Anitescu, S. P. A. Bordas, and T. Rabczuk, “Isogeometric analysis: An overview and computer implementation aspects,” *Math. Comput. Simul.* **117**, 89–116 (2015).
- ³⁷C. De Boor, “Package for calculating with B-splines,” *SIAM. J. Numer. Anal.* **14**, 441–472 (1977).
- ³⁸A. R. Khoei, S. O. R. Biabanaki, and M. Anahid, “A Lagrangian-extended finite-element method in modeling large-plasticity deformations and contact problems,” *Int. J. Mech. Sci.* **51**, 384–401 (2009).
- ³⁹J. C. Simo and T. J. R. Hughes, *Computational Inelasticity* (Springer Science & Business Media, 2006).
- ⁴⁰X. Du, G. Zhao, W. Wang, M. Guo, R. Zhang, and J. Yang, “NLIGA: A MATLAB framework for nonlinear isogeometric analysis,” *Comput. Aided. Geom. D.* **80**, 101869 (2020).
- ⁴¹J. P. Xu and S. Rajendran, “A ‘FE-Meshfree’ TRIA3 element based on partition of unity for linear and geometry nonlinear analyses,” *Comput. Mech.* **51**, 843–864 (2013).
- ⁴²S. Rajendran, B. R. Zhang, and K. M. Liew, “A partition of unity-based ‘FE-Meshfree’ QUAD4 element for geometric non-linear analysis,” *Int. J. Numer. Methods Eng.* **82**, 1574–1608 (2010).
- ⁴³X. Chen, W. Chen, J. Xu, W. Tu, S. Rajendran, and J. Lu, “An unsymmetric 8-node plane element immune to mesh distortion for linear isotropic hardening material,” *Int. J. Numer. Methods Eng.* **122**, 5540–5557 (2021).
- ⁴⁴F. Dunne and N. Petrinic, *Introduction to Computational Plasticity* (Oxford University Press, 2005), <https://global.oup.com/booksites/content/9780198568261>.
- ⁴⁵N.-H. Kim, *Introduction to Nonlinear Finite Element Analysis* (Springer Science & Business Media, 2014).
- ⁴⁶P. Papadopoulos and R. L. Taylor, “A mixed formulation for the finite element solution of contact problems,” *Comput. Methods Appl. Mech. Eng.* **94**, 373–389 (1992).
- ⁴⁷Y. Yang and H. Zheng, “Direct approach to treatment of contact in numerical manifold method,” *Int. J. Geomech.* **17**, 4016012 (2017).
- ⁴⁸D. Xu, A. Wu, Y. Yang, B. Lu, F. Liu, and H. Zheng, “A new contact potential based three-dimensional discontinuous deformation analysis method,” *Int. J. Rock. Mech. Min.* **127**, 104206 (2020).
- ⁴⁹P. L. Gould and Y. Feng, *Introduction to Linear Elasticity* (Springer, 1994).
- ⁵⁰J. Kim, J.-C. Yoon, and B.-S. Kang, “Finite element analysis and modeling of structure with bolted joints,” *Appl. Math. Model.* **31**, 895–911 (2007).
- ⁵¹Y.-F. Lyu, Y.-B. Wang, G.-Q. Li, and J. Jiang, “Numerical analysis on the ultimate bearing resistance of single-bolt connection with high strength steels,” *J. Constr. Steel. Res.* **153**, 118–129 (2019).
- ⁵²Y. Zhang, B. Chen, A. Liu, Y.-L. Pi, J. Zhang, Y. Wang, and L. Zhong, “Experimental study on shear behavior of high strength bolt connection in pre-fabricated steel-concrete composite beam,” *Composites, Part B* **159**, 481–489 (2019).
- ⁵³M. Thome, G. Hirt, and B. Rattay, “Metal flow and die filling in coining of micro structures with and without flash,” *Adv. Mat. Res.* **6–8**, 631–638 (2005).
- ⁵⁴G. C. Randall, J. Dahal, J. Vecchio, S. Agarwal, R. Mehta, G. Ravichandran, and A. P. Stebner, “Microcoining ripples in metal foils,” *Int. J. Mech. Sci.* **148**, 263–271 (2018).